Topology of many-body edge and extended quantum states in an open spin chain: 1/3 plateau, Kosterlitz-Thouless transition, and Luttinger liquid

R. R. Montenegro-Filho,[1] F. S. Matias,[1,2] and M. D. Coutinho-Filho[1]
[1]*Laboratório de Física Teórica e Computacional, Departamento de Física, Universidade Federal de Pernambuco, 50760-901 Recife-PE, Brazil*
[2]*Instituto de Física, Universidade Federal de Alagoas, 57072-970 Maceió-AL, Brazil*

(Received 1 May 2020; revised 25 June 2020; accepted 6 July 2020; published 20 July 2020)

Quantum many-body edge and extended magnon excitations from the 1/3 plateau of the anisotropic Heisenberg model on an open AB_2 chain in a magnetic field h are unveiled using the density matrix renormalization group and exact diagonalization. By tuning both the anisotropy and h in the rich phase diagram, the edge states penetrate in the bulk, whose gap closes in a symmetry-protected topological Kosterlitz-Thouless transition. Also, we witness the squeezed chain effect, the breaking of the edge state degeneracy, and a topological change of the excitations from gapped magnons with quadratic long-wavelength dispersion to a linear spinon dispersion in the Luttinger liquid gapless phase as the anisotropy λ approaches the critical point from the $\lambda > 0$ side of the phase diagram.

DOI: 10.1103/PhysRevB.102.035137

I. INTRODUCTION

Recently, increasing experimental and theoretical attention was given to topological aspects of condensed matter physics [1]. In one-dimensional (1D) systems, an early essential role of topology was provided by the so-called *Haldane conjecture* [2,3]: the ground state of integer (half-integer) spin chains is gapped (gapless). In fact, the conjecture was experimentally verified in spin-1 chains [4]; further, density matrix renormalization group (DMRG) studies confirmed that the *bulk* gapped ground state displays spin-1/2 fractionalized *edge* states in open chains [5]. Topological insulators [6] share with these systems some general aspects [7]: an insulating bulk and a conducting surface (edge states) are intrinsically connected, a phenomenon known as bulk-boundary correspondence. The Su-Schrieffer-Heeger (SSH) dimerized model [8], and trimer models [9], including a diamond chain [10], are examples of models that manifest the bulk-boundary correspondence in regions of their parameter space. In addition, the phonon structures arising from mechanical isostatic [11] and Maxwell [12] lattices can be understood from the similar framework of topological band theory of electronic systems, including the bulk-boundary correspondence. Also, chiral magnonic edge states in ferromagnetic skyrmion crystals controlled by magnetic fields were reported [13]. In addition, we mention that the association of a two-dimensional Chern number with a one-dimensional system was also suggested for photonic quasicrystals [14] and fermionic systems in quasiperiodic optical superlattices [9,15].

Gapped ground states of spin chains, either with spin-1 or more complex unit cells with spin-1/2 sites, imply plateaus in the magnetization (m) curves as a function of the magnetic field (h): $m(h)$. This is a topological quantization of the magnetization due to the presence of h, analogously to the quantum Hall effect [16]. Recently, this issue was investigated in modulated spin chains [17], with particular attention to the edge states of open systems. On the other hand, a magnetization plateau at 1/3 of the saturation magnetization (1/3 plateau) has been observed in several model systems. The isotropic AB_2 chain exhibits a ferrimagnetic ground state [18–21] and the 1/3 plateau in $m(h)$ [22,23]. The topological nature of the ground state manifests in topological Wess-Zumino terms of the nonlinear sigma model [21] or through its representation on a valence-bond state basis [24]. Likewise, the spin-(1/2,1) and spin-(1/2,5/2) alternating spin chains also exhibits a ferrimagnetic ground state, together with the 1/3 plateau [20,25–27] and the 2/3 plateau [28], respectively. In addition, we mention the 1/3 plateau state of the quantum spin-1/2 XX diamond chain in a magnetic field [29]. Further, in the phase diagram of anisotropic spin models, the 1/3 plateau closes in a transition of the Kosterlitz-Thouless (KT) type [30] as the anisotropy changes [31,32]. The KT transition is also observed in anisotropic ferrimagnetic branched chains [33,34]. On the experimental side, the 1/3 plateau was observed in materials with three spin-1/2 sites per unit cell (diamond chain): the mineral azurite $Cu_3(CO_3)_2(OH)_2$ [35], and the compounds copper hydroxydiphosphate $Cu_3(P_2O_6OH)_2$ [36] and alumoklyuchevskite $K_3Cu_3AlO_2(SO_4)_4$ [37]. Also, the 2/3 plateau was observed in a new mixed spin-(1/2,5/2) chain in a charge-transfer salt (4-Br-*o*-MePy-V)$FeCl_4$ [38].

In this work, DMRG and exact diagonalization (ED) results for open and closed anisotropic Heisenberg-AB_2 chains, respectively, unveil a very rich phase diagram and related notable features. In particular, in open chains we identify a secondary plateau associated with edge and extended magnon excitations from the 1/3 plateau. We stress that the edge magnon states that emerge from this plateau are many-body quantum states. As one approaches the symmetry-protected [translational and $U(1)$ symmetries] topological quantum KT transition, the bulk penetration of the edge states is enhanced,

their degeneracy is broken, and the squeezed chain effect is observed. Further, at the KT transition and beyond, the bulk magnon gap closes, while the edge states mix with the continuum, and the Luttinger liquid (LL) excitations dominate the scenario.

In Sec. II, we discuss the topology and phase diagram of the anisotropic Heisenberg-AB_2, and a precise determination of the KT transition point. The edge states associated with the 1/3 plateau are considered in Sec. III, while gapped and gapless excitations around the topological KT transition are discussed in Sec. IV. The boundary scattering length for the 1/3 plateau and the magnon-magnon scattering length for the fully polarized (FP) plateau magnons are reported in Sec. V. A summary and conclusions are found in Sec. VI.

II. TOPOLOGY AND PHASE DIAGRAM

The anisotropic Heisenberg model on the AB_2 chain in an applied magnetic field h reads

$$H = \sum_{i=1}^{N_c} \left[S^x_{A,i}\left(S^x_{B,i} + S^x_{B,i-1}\right) + S^y_{A,i}\left(S^y_{B,i} + S^y_{B,i-1}\right) + \lambda S^z_{A,i}\left(S^z_{B,i} + S^z_{B,i-1}\right)\right] - hS^z, \quad (1)$$

where $S^{x,y,z}_{B,i} = S^{x,y,z}_{B_1,i} + S^{x,y,z}_{B_2,i}$, N_c is the number of unit cells of the system, the exchange couplings in the xy plane define the unit of energy, λ is the exchange coupling in the z-direction, and $S^z = \sum_{i=1}^{N_c}(S^z_{A,i} + S^z_{B_1,i} + S^z_{B_2,i})$ is the z component of the total spin of the system, as illustrated in Fig. 1(a). We use DMRG to study open chains of N_c unit cells, with one A site at each boundary, retaining 243 states per block and performing 12 sweeps in each calculation, such that the higher discarded weight was of order 10^{-9}. We also study closed systems with $N_c = 10$ and 12 through ED. The magnetization curves are obtained from the lowest energy in each total spin S^z sector and $h = 0$: $E(S^z)$, since the Zeeman term in the Hamiltonian (1) implies $E_h(S^z) = E(S^z) - hS^z$ for $h \neq 0$. In a finite-size system, the $m(h)$ curve is composed of finite-size steps of width $\Delta h(S^z)$ at total spin S^z. Considering h_{S^z+} and h_{S^z-} as the extreme points of these steps, such that $\Delta h(S^z) = h_{S^z+} - h_{S^z-}$, we thus have $h_{S^z\pm} = \pm[E(S^z \pm 1) - E(S^z)]$. If S^z is not at a thermodynamic-limit magnetization plateau state, we have $\Delta h(S^z) \to 0$ as $N_c \to \infty$, otherwise $\Delta h(S^z) \neq 0$ as $N_c \to \infty$.

In Fig. 1(b) we present DMRG results ($N_c = 121$) for $m(h)$ and the anisotropy in the interval $-0.9 \leqslant \lambda \leqslant 1$. The $m(h)$ curves display the FP plateau at the thermodynamic-limit (bulk) saturation magnetization $m_s = 3/2$, a plateau slightly below the bulk 1/3 plateau at $m_s/3 = 1/2$, and a secondary plateau, as shown in the inset for $\lambda = 1.0$. The fields h_-, h_0, and h_+ define the width of the plateaus: the secondary one is associated with edge and extended magnon excitations from the 1/3 plateau. Here, these excitations will be examined in detail around the KT transition, in which case LL excitations also take place. In fact, in Fig. 1(c), a rich h-λ phase diagram exhibits the various phases that play a significant role in our analysis.

In bulk, without broken translational symmetry, the possible occurrence of a plateau in $m(h)$ must satisfy the topological criterion [16]:

$$S_c - m = \text{integer}, \quad (2)$$

where S_c is the maximum spin of a unit cell. In our model, $S_c = 3/2$, $m = 1/2$ for the 1/3 plateau, and $m = 3/2$ for the FP plateau. Also, this topological criterion can be related [17] to a Chern number C_m defined in the two-dimensional parameter space of an associated periodically modulated closed system under a twisted boundary condition. Indeed, an m-plateau obeys the relation

$$C_m = -(S_c - m) \quad (3)$$

for $m \geqslant 0$, with $C_m = -C_{-m}$ for $m < 0$, i.e., $h < 0$ not shown in Fig. 1. Thus, the FP plateau has a Chern number $C_{3/2} = 0$ and is a trivial insulating state, while the 1/3 plateau is a

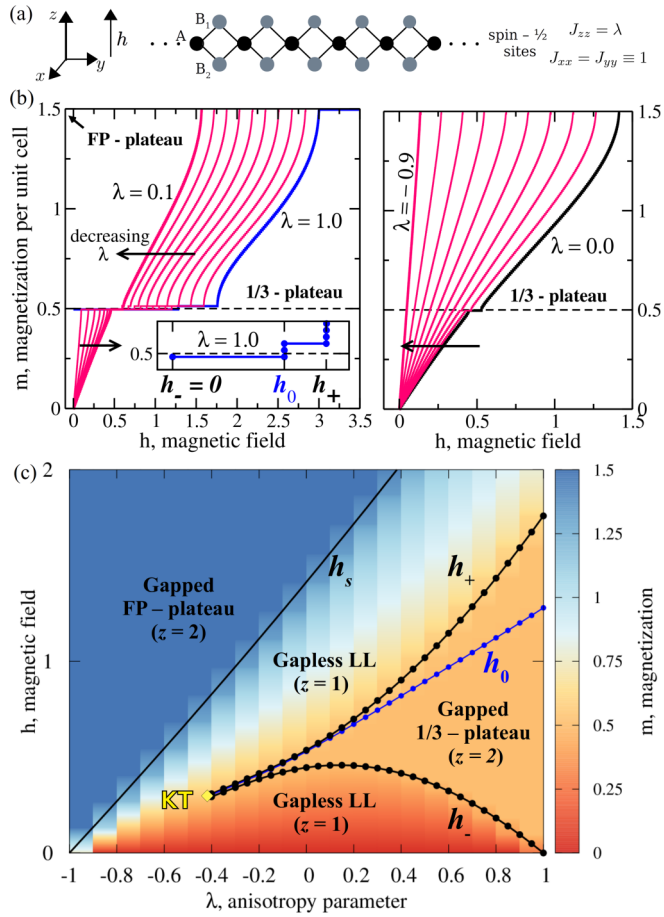

FIG. 1. (a) Schematic representation of the anisotropic Heisenberg Hamiltonian on the AB_2 spin-1/2 chain, under a magnetic field h. DMRG results for the open AB_2 chain with $N_c = 121$ unit cells: (b) Magnetization per unit cell $m(h)$ for $1 \geqslant \lambda \geqslant 0.1$ (left panel) and $0.0 \geqslant \lambda \geqslant -0.9$ (right panel), in steps of $\Delta\lambda = 0.1$. Inset of the left panel: $m(h)$ for $\lambda = 1.0$ in the vicinity of the 1/3 plateau bounded by $h_- = 0$ and $h_+ = 1.76$, with a step at $h_0 = 1.28$; (c) phase diagram: the color code refers to the m values in (b). The exact critical line h_s bounds the FP plateau, while h_-, h_0, and h_+ are related to the 1/3 plateau. The gapped phases, with dynamical exponent $z = 2$, are separated by the gapless Luttinger liquid (LL) phase with $z = 1$. The 1/3 plateau closes at a Kosterlitz-Thouless (KT) transition: $\lambda_{KT} = -0.419 \pm 0.004$ and $h_{KT} = 0.290 \pm 0.002$.

topological insulator with $C_{1/2} = -1$. In Sec. V B, we present a detailed discussion of the trivial insulating FP plateau state.

In our open finite-size chain, a remarkable feature is the presence of edge states, leading to the splitting of the 1/3 plateau into two plateaus. Consider, for example, the isotropic case shown in the inset of Fig. 1(b). The bulk 1/3 plateau has extreme points at $h_- = 0$ and $h_+ = 1.76$ [for both spin-(1/2,1) [39] and AB_2 [22] chains]. However, in the open finite-size system and $h_0 \leqslant h < h_+$, the magnon excitations occupy edge states inside the gap between the lower and upper bulk band states and give rise to the two plateaus in $m(h)$. The transition between these two plateaus occurs at $h_0 = 1.28$ for $\lambda = 1$.

The phase diagram of the AB_2-chain with $N_c = 121$ unit cells is shown in Fig. 1(c). The extreme lines of the bulk plateaus, $h_-(\lambda)$, $h_+(\lambda)$, and $h_s(\lambda)$, are quantum critical lines separating a gapped insulating phase from the gapless LL phase, with dynamic critical exponent $z = 2$ and 1, respectively. The FP plateau is bounded by $h_s(\lambda) = \frac{3\lambda}{2} + \frac{1}{2}\sqrt{8+\lambda^2}$, since the energy of the exact Goldstone mode (a $\Delta S^z = -1$ magnon) associated with this line reads $\varepsilon_{\rm FP}(k) = -\frac{3\lambda}{2} - \frac{1}{2}\sqrt{\lambda^2 + 8\cos^2(k/2)} + h$. Therefore, for h close to $h_s(\lambda)$, a high-dilute regime of magnons is verified, with the following low-lying excitation energy:

$$\varepsilon(k) = -\mu + \frac{v^2 k^2}{2h_s}, \tag{4}$$

where $\mu = h_s - h$ and the spin-wave velocity is

$$v = \frac{1}{\sqrt{2\left(1 - \frac{3\lambda}{2h_s}\right)}}. \tag{5}$$

In addition, the 1/3 plateau is bounded by the critical lines $h_-(\lambda)$ and $h_+(\lambda)$, with a width $\Delta(\lambda) = h_+(\lambda) - h_-(\lambda)$. The plateau width $\Delta(\lambda)$ is the *bulk gap* that separates the two regions of the gapless LL phase: one with $m < 1/2$ and the other with $m > 1/2$, for the same value of λ. On the other hand, the low-energy theory of magnons in a gapped system under a magnetic field is that of a Lieb-Liniger [40] Bose fluid with δ-function interactions [41]. In addition, in the high dilute regime of magnons, the theory is equivalent to a Tonks-Girardeau [42] Bose system with a hard-core repulsion [41] or a fermionic system [28,41,43,44]. Thereby, in the high-dilute regime $h \to h_-$ or h_+, the low-energy magnon excitations from the 1/3 plateau have dispersion relations as in Eq. (4), with $\mu = \pm(h - h_\pm)$. For $h \lesssim h_-$, the magnons carry spin $\Delta S^z = -1$, while for $h \gtrsim h_+$, the excitations carry spin $\Delta S^z = +1$. The $\Delta S^z = -1$ excitations can thus be understood as holes, in the reciprocal q-space, in a filled band of $\Delta S^z = +1$ hard-core magnons, and the bulk gap $\Delta(\lambda)$ is the particle-hole gap. The plateau closes at the KT quantum critical point: $\lambda_{\rm KT} = -0.419 \pm 0.004$ and $h_{\rm KT} = 0.290 \pm 0.002$, estimated through the procedure described below.

A. Kosterlitz-Thouless transition point: $\lambda_{\rm KT}$ and $h_{\rm KT}$

In the LL gapless phase shown in Fig. 1(c), the transverse spin correlation function should obey the asymptotic power-law behavior given by [45]

$$\Gamma(r) \sim \frac{1}{r^{\frac{1}{2K}}}, \tag{6}$$

where r is the distance between spins and K is the Luttinger liquid parameter K, which depends on h (or m) and λ. In the Kosterlitz-Thouless transition, the magnetization has the fixed value $m = 1/2$ and the transition is induced by changing λ. In this case, $K = 2$ at the critical point $\lambda = \lambda_{\rm KT}$.

We estimate the value of $\lambda_{\rm KT}$ through a method successfully used to estimate the KT transition points in a one-dimensional Bose-Hubbard model in Ref. [46]. In our case, the procedure consists in identifying the values of λ at which $K = 2$ for $m = 1/2$ in finite size systems, and extrapolating the results to $N_c \to \infty$. We calculate the transverse spin correlation functions as

$$\Gamma(r) \equiv \langle\langle S^+(l) S^-(l+r)\rangle\rangle_l, \tag{7}$$

where the $\langle\langle \cdots \rangle\rangle_l$ indicate the quantum expectation value and an average of the correlation over all pairs of cells with a distance l between then, in order to minimize the effects of the open boundaries of the chain.

In Fig. 2(a), we show $\Gamma(r)$ between A spins for $\lambda = -0.5$ and $N_c = 121$, 181, and 241 at $m = 1/2 - (1/2N_c)$. For each system size, we fit the data in different intervals of r to the asymptotic expression in Eq. (6). The following intervals were considered for r: [1,8], [1,16], [1,60], [16,32], and [32,48] for values of λ around the KT transition. In particular, in Fig. 2(b) we show K as a function of the system size for $\lambda = -0.5$ and the chosen r-intervals. We see that a straight line can be a good scale function for K in all studied r-intervals. Hence, we fit a linear function to the data of the two largest system sizes in order to obtain a very confident extrapolated value of K, i.e., with very little dispersion. Indeed, for the case shown in Fig. 2(b), $\lambda = -0.5$, the extrapolated value of K is in the range 2.218 ± 0.006. In Fig. 2(c), we show the extrapolated values of K as a function of λ for each of the chosen r-intervals. The KT critical value of λ,

$$\lambda_{\rm KT} = -0.419 \pm 0.004, \tag{8}$$

is estimated by considering the minimum and maximum values of λ at which $K = 2$, in all chosen r-intervals. The bulk gap $\Delta(\lambda)$ nullifies following an essential singularity form

$$\Delta(\lambda) = A \exp \frac{B}{\sqrt{\lambda - \lambda_{KT}}}, \tag{9}$$

where A and B are constants. In Fig. 2(d) we show a scale analysis of the plateau width for some values of λ in the gapped phase. In Fig. 2(e), we present the extrapolated values of the bulk gap as a function of λ and the fitting of them to the expression (9).

The value of the critical field $h_{\rm KT}$ can be estimated by a scaling analysis of the extreme fields h_- and h_+ of the finite-size 1/3-plateau magnetization at $m = 1/2 - (1/2N_c)$. In Fig. 3, we present h_- and h_+ as a function of system size for the minimum and maximum values of $\lambda_{\rm KT}$: -0.415 and -0.423. In both cases, an excellent linear scale function fits the data for h_- and h_+. For $\lambda = -0.415$, the extrapolated values of h_- and h_+ differ by 7×10^{-5}, while for $\lambda = -0.419$ the difference is 5×10^{-5}. We estimate the critical field of

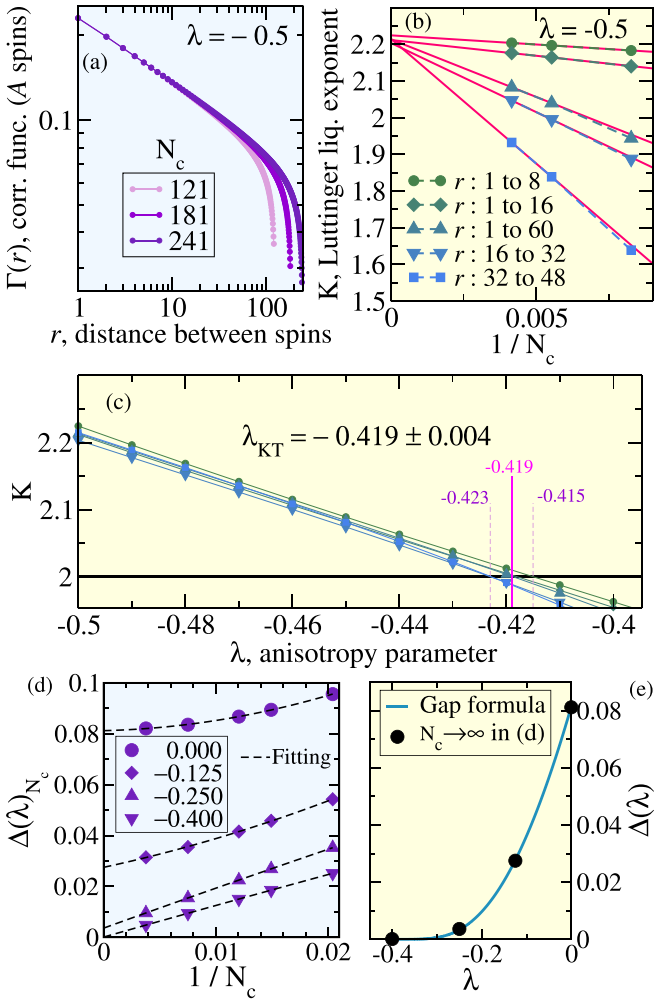

FIG. 2. Critical λ of the Kosterlitz-Thouless transition: λ_{KT}. (a) Transverse spin correlation functions $\Gamma(r) = \langle\langle S^+(l)S^-(l+r)\rangle\rangle_l$ between A spins as a function of distance r for $\lambda = -0.5$ at the magnetization (m) of the 1/3 plateau: $m = (1/2) - (1/2N_c)$ for the number of unit cells indicated. For a given system size, $\Gamma(r)$ is calculated by averaging over all pairs of spins separated by the distance r. (b) Luttinger liquid exponent K as a function of $1/N_c$ for the three system sizes shown in (a) and $\lambda = -0.5$. The value of K is determined by fitting $\Gamma(r)$ to the expected long-distance power-law behavior $1/r^{1/2K}$ through the indicated intervals of r. Full lines are linear extrapolations of K to $N_c \to \infty$ by considering the two highest system sizes. (c) Extrapolated value of K as a function of λ for each fitting interval indicated in (b). The critical λ is estimated from the minimum and maximum values of λ at which $K = 2$, within the set of investigated fitting intervals. (d) 1/3 plateau width $\Delta(\lambda)_{N_c}$ as a function of $1/N_c$ for the indicated values of λ; dashed lines are fittings to a polynomial expression. (e) (•) $\Delta(\lambda)$ from (d) as a function of λ. The full line is the fitting of these data to the essential singularity formula $A \exp(B/\sqrt{\lambda - \lambda_{KT}})$.

the KT transition, h_{KT}, as the range from the extrapolated value of h_- at $\lambda = -0.423$ to the extrapolated value of h_+ at $\lambda = -0.415$, thus obtaining

$$h_{KT} = 0.290 \pm 0.002. \tag{10}$$

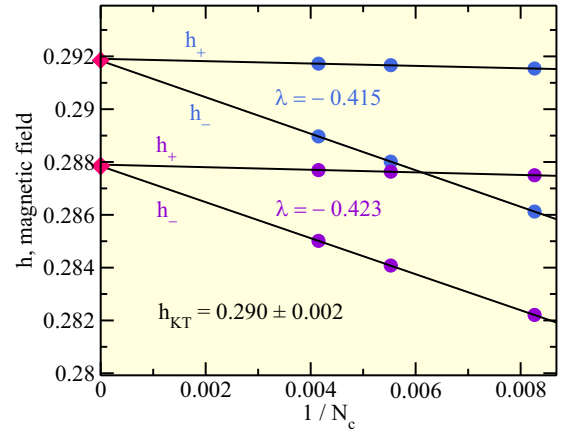

FIG. 3. Critical h of the KT transition: h_{KT}. Extreme fields of the finite-size 1/3 plateau magnetization: $m = (1/2) - (1/2N_c)$, as a function of $1/N_c$ for $\lambda = -0.415$ and -0.423, which are the estimated minimum and maximum values of λ at the KT transition. For each value of λ, we use a linear extrapolation in $1/N_c$ to evaluate the thermodynamic value of h for $m = 1/2$. The critical field is estimated as the average of the extrapolated values.

The AB_2 anisotropic chain is invariant under the exchange of the two B sites of a unit cell, so the Hamiltonian does not connect the singlet and triplet states of these pairs. The localized singlet pairs appear in higher-energy states of the system that are not activated by either the magnetic field nor the anisotropy. Thus, the h versus λ phase diagram of the AB_2 anisotropic chain is the same as that of the alternating spin-(1/2,1) anisotropic chain [31,32], and we can compare the results for this chain with our estimates for $\lambda_{KT} = -0.419 \pm 0.004$ and $h_{KT} = 0.290 \pm 0.002$. These values disagree with the ones suggested for the anisotropic alternating chain in Ref. [32] by observing the behavior of the two-site entanglement calculated by the infinite time-evolving block-decimation (iTEBD) algorithm: $\lambda = -0.53$ and $h = 0.23$. On the other hand, the values estimated in Ref. [31] through a finite-size analysis of the central charge and plateau size: $\lambda = -0.41 \pm 0.01$ and $h = 0.293$, are compatible with our more precise results.

III. EDGE MAGNON EXCITATIONS OF THE GAPPED 1/3 PLATEAU

In our open chain, the topological quantum phase transition from the insulating ($z = 2$) to the metallic phase ($z = 1$) manifests in the penetration into the bulk of the edge (surface) states [47]. We start by discussing the magnon edge states associated with the topological insulator at the 1/3 plateau in the open AB_2-chain of size $N_c = 121$ and $\lambda = 0.4$. In Fig. 4(a) we present $m(h)$ in the vicinity of the 1/3 plateau ($m = 0.5$ in the thermodynamic limit). In this finite-size system, the m-states that characterize the 1/3-plateau phase are labeled by ① ($m = 60/121$), ② ($m = 61/121$), and ③ ($m = 62/121$), while the first extended state above the plateau is labeled by ④ ($m = 63/121$). As m changes from a state ① to a state ⓕ, the change in the average distribution of $\Delta S^z = +1$ magnons on sites A, $\langle n_A\rangle$, and sites $B = B_1 + B_2$, $\langle n_B\rangle$, is calculated through $\langle n_X\rangle_{①\to ⓕ} = \langle S^z_X\rangle_f - \langle S^z_X\rangle_i$, with

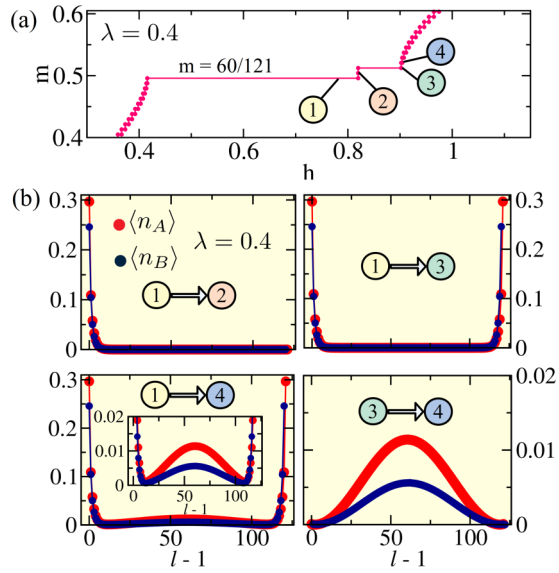

FIG. 4. DMRG results for $m(h)$ and the average magnon distribution along the AB_2 open chain with $N_c = 121$ at $\lambda = 0.4$. (a) $m(h)$ in the vicinity of the 1/3 plateau displaying the indicated m-states: ① ($m = 60/121$), ② ($m = 61/121$), and ③ ($m = 62/121$), and the first gapless m-state above the plateau (onset of the continuum): ④ ($m = 63/121$). (b) Average magnon distribution at sites A, $\langle n_A\rangle$, and B, $\langle n_B\rangle \equiv \langle n_{B_1}\rangle + \langle n_{B_2}\rangle$, as a function of cell position $l - 1$. Excitations ① → ②, ① → ③, and ① → ④ create one, two, and three magnons above the m-state ①, while ③ → ④ creates one magnon in the m-state ③.

$X = A$ or B, as shown in the panels of Fig. 4(b). In panel ① → ②, the magnon distribution indicates that a magnon added to the state ① is localized at the left edge of the chain, while a second magnon added to ①, panel ① → ③, is localized at the right edge. Thus, the distributions of one- and two-magnon states above ① indicate the presence of localized states at both edges of the chain, implied by the inversion symmetry of the finite-size chain relative to its center, with the density on A sites higher than those on B sites. Concerning the three-magnon state, panel ① → ④ in Fig. 4(b), the magnon distribution evidences that the third magnon occupies a metallic state, which extends throughout the bulk. Indeed, panel ③ → ④ in Fig. 4(b) presents the distribution of this one-magnon extended state, which is clearly isolated from the edge states. In Appendix A we show that the magnetization and magnon distributions for an even number of unit cells and the same boundary conditions have the same physical features, while using a boundary condition with a B_1, B_2 at one extreme gives rise to only one edge state. Further, in Appendix B we present the average local magnetizations along the chain, from which the magnon distributions were calculated.

Now, we shall focus on the very interesting behavior of edge and bulk magnon excitations as the 1/3 plateau gets closer to the KT critical point: λ_{KT}, h_{KT}. In Fig. 5 (semilog plots), we present the average distributions of one (① → ②) and two (① → ③) magnon excitations above ①, as well as the isolated one-magnon extended state (excitation ③ → ④), for $\lambda = 0.1$, 0.0, and -0.1, corresponding to the first, second, and third columns, respectively. For $\lambda = 0.1$ (first column) the

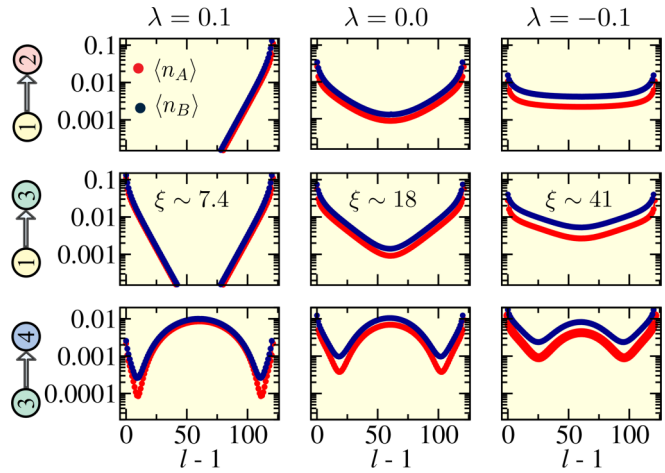

FIG. 5. DMRG results for the average magnon distributions $\langle n_A\rangle$ and $\langle n_B\rangle$ along the AB_2 open chain with $N_c = 121$ as the KT transition gets closer. A log-normal scale is used in the figures. The panel columns are data for $\lambda = -0.1$, 0.0, and 0.1, from left to right, while panel lines show $\langle n_A\rangle$ and $\langle n_B\rangle$ for the ① → ②, ① → ③, and ③ → ④ excitations. The localization length ξ shown in the second line of the panels is obtained by fitting the data of $\langle n_A\rangle$ in the range $30 \leqslant x \leqslant 40$ to $e^{-x/\xi}$, with cell position $x = l - 1$.

one-magnon state is exponentially localized at the right edge, while the two-magnon state displays one localized magnon at each edge, similarly to the $\lambda = 0.4$ case in Fig. 4(b). Thus, left and right edge states are still degenerate. However, at $\lambda = 0$ (second column), the gap between the two edge states [$\equiv \Delta h = 6 \times 10^{-4}$, as shown in Fig. 6(a)] is open and the one-magnon state displays a symmetrical density on *both edges* of the chain due to hybridization, thus leading to bulk penetration. Also, the two-magnon state exhibits similar behavior with a small dip at the center of the chain. Further,

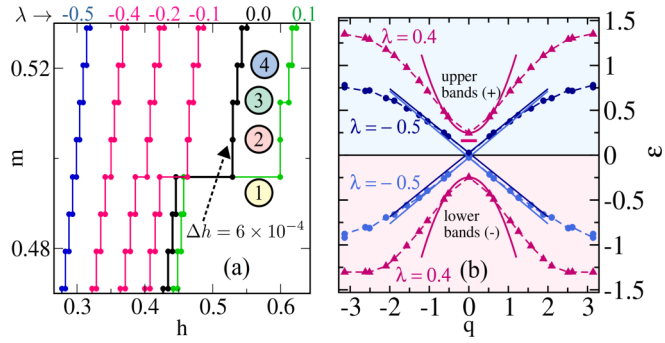

FIG. 6. (a) DMRG results for $m(h)$ in the vicinity of the 1/3 plateau of the AB_2 open chain with $N_c = 121$ for the indicated values of λ and the indicated m-states: ① ($m = 60/121$), ② ($m = 61/121$), ③ ($m = 62/121$), and ④ ($m = 63/121$), as in Fig. 4. Notably, for $\lambda = 0.0$, there is a finite-size step of size $\Delta h = 6 \times 10^{-4}$ at the m-state ②. (b) Upper and lower band energies for $\Delta S^z = +1$ magnons of wave-vector q, with h at the center of the 1/3 plateau, $(h_+ + h_-)/2$, for $\lambda = 0.4$ (▲) and -0.5 (●), using ED results from $N_c = 10$ and 12 under closed boundary conditions. We also indicate the twofold-degenerate magnon edge states (–) below the bottom of the magnon upper band, using DMRG for $\lambda = 0.4$ and an open chain with $N_c = 121$.

as shown in Fig. 5, as the bulk gap $\Delta(\lambda)$ (width of the 1/3 plateau) decreases, the localization length ξ of the edge states increases, since $\xi(\lambda) \sim 1/\Delta(\lambda)$, and the edge state becomes more extended. In fact, for $\lambda = -0.1$, the density profiles of one- and two-magnon edge states are very extended, with the density at the boundaries approaching their values in bulk. Using data from the excitation ① → ③ in Fig. 5 for $\lambda = 0.1$, 0.0, and -0.1, we have estimated the values of the localization length: $\xi = 7.4$, 18, and 41, respectively. On the other hand, for $\lambda = 0.1$, the weight at the boundaries of the isolated one-magnon extended state, excitation ③ → ④, is much higher than the practically negligible weight in the $\lambda = 0.4$ case [see Fig. 4(b)]. In fact, as the gap closes, the insulating bulk is squeezed, as shown in Fig. 5 by the decreasing of the distance between the two minima in the ③ → ④ excitation, and also by the increasing penetration of the edge states for the two-magnon ① → ③ state. Notably, far enough from the boundaries, the bulk wave function of the ③ → ④ one-magnon state is that of a squeezed chain of size $L - 2a_b$, where a_b is the boundary scattering length of an effective repulsive potential [48]. A more detailed quantitative discussion is presented in Sec. V A.

IV. GAPPED AND GAPLESS EXCITATIONS AROUND THE TOPOLOGICAL KT TRANSITION

In Fig. 6(a), we show $m(h)$ in the vicinity of the 1/3 plateau for the indicated values of λ and using the same state labeling of Figs. 4 and 5. A remarkable feature is the *breaking of the degeneracy* between states ② and ③ for $\lambda \sim 0.0$ (black curve), as one decreases λ from $\lambda = 0.1$ (green curve), in agreement with the magnon distribution in Fig. 5. In fact, for $\lambda = 0.0$ there is a gap of size 6×10^{-4} between these states, implying an m-step of width $\Delta h = 6 \times 10^{-4}$ in the m-state ②. Further, the width of the m-step increases (decreases) at the m-state ② (①) as the gap closes, and all states take part of the continuum at the KT critical point $(\lambda_{\rm KT}, h_{\rm KT})$ in the thermodynamic limit. Accordingly, in our finite-size system we observe uniformity in the values of the widths of the m-steps, as shown in Fig. 6(a) for $\lambda = -0.5$ (blue curve), a signature of a gapless LL phase.

In addition, a remarkable topological change in the dispersion relation of the low-energy magnetic excitations takes place around the KT critical point. There are two kinds of bulk magnetic excitations from the 1/3 plateau: one carrying a spin $\Delta S^z = +1$, which increases the 1/3-plateau total spin $S^z_{1/3}$ by one unit, and the other carrying a spin $\Delta S^z = -1$, which decreases $S^z_{1/3}$ by one unit. The excitations with $\Delta S^z = -1$ can be understood as a hole, in the reciprocal q-space, in a filled band of $\Delta S^z = +1$ excitations. The magnetic field acts as a chemical potential: for $h = h_-$ the lower band is filled and the upper one is empty; increasing h, the magnetization does not change (plateau region) up to $h = h_+$, at which the upper band starts to be filled. Defining $E_{1/3}$ as the total energy of the 1/3-plateau magnetization and $h = 0$, the energy $\varepsilon_\pm(q)$ of the upper (+) and lower (−) bands is given by

$$\varepsilon_\pm(q) = \pm[E_\pm(q) - E_{1/3}] - h, \tag{11}$$

where $E_+(q)$ and $E_-(q)$ are the lowest total energy at the sector q for $S^z = S^z_{1/3} + 1$ and $S^z = S^z_{1/3} - 1$, respectively, with $h = 0$. In Fig. 6(b) we show $\varepsilon_\pm$ for a closed system with $N_c = 10$ and 12, and $h = (h_+ + h_-)/2$ for $\lambda = 0.4$ (gapped magnon in the 1/3-plateau phase) and $\lambda = -0.5$ (gapless spinon in the LL phase). The expected [41,43,49] long-wavelength behavior is also sketched with full lines. For $h_- < h < h_+$ (inside the 1/3 plateau), the excitations should obey a quadratic dispersion relation [41,43,49]

$$\varepsilon_\pm(q) \to h_\pm \pm \frac{v_\pm^2}{2h_\pm} q^2 - h \text{ as } q \to 0, \tag{12}$$

where $v_\pm$ are the spin-wave velocities (see the discussion in Sec. II). For $\lambda = 0.4$, shown in Fig. 6(b), a fitting (full lines) gives $v^2/2h \approx 0.61$ (0.62) for the upper (lower) band. On the other hand, in the gapless LL phase, the upper and lower bands are joined at $q = 0$, and the excitations follow a linear dispersion relation

$$\varepsilon_\pm(q) \to \pm v_s|q| \text{ as } q \to 0, \tag{13}$$

where v_s is the spinon velocity.

V. BOUNDARY AND MAGNON-MAGNON SCATTERING LENGTHS

A. Boundary scattering length for magnon excitations from the 1/3-plateau magnetization

Here, we consider the average density profile of the isolated extended magnon excitation, obtained from the magnetization change ③ → ④, as described in Sec. III. In our open chain, the bulk magnon lives on a squeezed chain with size [48] $N_c - 2a_b$, where the *boundary scattering length* a_b accounts for the repulsive ($a_b > 0$) boundary potentials. Thereby far enough from the boundaries, the bulk single-particle wave functions in the open chain can be written as [48]

$$\psi_p(x) = \sqrt{A} \sin\left[\frac{p\pi(x - a_b)}{(N_c - 2a_b)}\right], \tag{14}$$

where $p = 1, 2, \ldots$ and A is a constant. In Fig. 7 we fit the DMRG data for the chain with $N_c = 121$ unit cells to the expression in Eq. (14) with $p = 1$, and we obtain $a_b = 0.6$, 8.0, and 18.0 for $\lambda = 1.0$, 0.1, and -0.1, respectively.

B. Fully polarized plateau: Insulator with trivial topology, and magnon-magnon scattering length

The fully polarized plateau is an example of a topological trivial insulator, with a Chern number $C_{3/2} = 0$ (see the discussion in Sec. II). Thus, in an open chain, the fully polarized state does not have edge states. Below we present the bulk magnon excitations from the fully polarized plateau, including the linear correction for the square-root law, and we discuss the magnon density profile for two magnons in an open chain.

In Fig. 8(a) we present the two-particle average magnon density along the chain for the fully polarized plateau, $\langle n_l \rangle$. For comparison, we show the free fermion density for two fermions in a chain of size $N_c - 1$ and vanishing boundary condition:

$$\frac{2}{N_c - 1}\left[\sin^2\left(\frac{\pi x}{N_c - 1}\right) + \sin^2\left(\frac{\pi x}{N_c - 1}\right)\right], \tag{15}$$

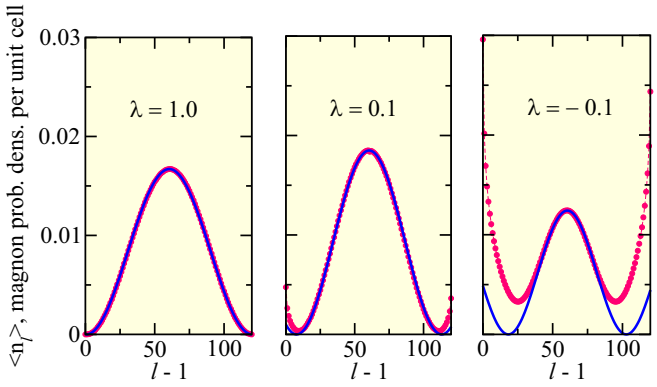

FIG. 7. Average magnon density $\langle n_l \rangle$ per unit cell along the chain for the extended one-magnon excitation in the 1/3-plateau state. (•) DMRG results for $N_c = 121$. The full line is a fitting of the DMRG data to the continuum limit expression for the probability density (far from the boundaries) of a particle in a box with a finite potential at the boundaries: $A \sin^2[\pi(x - a_b)/(N_c - 2a_b)]$, where a_b parametrizes the interaction with the boundaries, A is a fitting parameter, and $x = l - 1$. The fitting is done using the data in the range $x = 45$–75.

with $x = l - 1$. We notice the absence of edge states in this case for $-0.9 \leqslant \lambda \leqslant 1.0$. A tiny departure from the free fermion result is observed as $\lambda \to -1$, the critical ferromagnetic point. The average magnon density increases at the boundaries with a decrease in the central region as $\lambda \to -1$. We explain it by noticing that if a $\Delta S^z = -1$ magnon is at a boundary A site, with the other sites fully polarized, the value of the longitudinal term of the energy is $-\lambda$. If the magnon is not at a boundary site, this energy term is -4λ (at a B_1 or B_2 site) or -2λ (at an A site). Hence, for $\lambda < 0$ the effect of the boundaries is represented by an attractive potential at the chain ends. However, while in Fig. 7 we can observe a crossover between the profiles at the center and at the boundaries of the chain, this crossover is not evidenced in the density profiles shown in Fig. 8(a).

In the high-dilute limit of magnons near the $h_s(\lambda)$ line, the bulk magnon density per unit cell is given by

$$n = \sqrt{\frac{2h_s\mu}{\pi^2 v^2}}, \tag{16}$$

with $n = m_{\mathrm{FP}} - m$, $\mu = h_s - h$, and v in Eq. (5). Including the linear first correction [48,50–53] to the square-root law, the magnon density becomes

$$n = \sqrt{\frac{2h_s}{\pi^2 v^2}}\sqrt{\mu} - a\frac{4}{3}\frac{2h_s}{\pi^2 v^2}\mu, \tag{17}$$

where a is the magnon-magnon scattering length, which can be positive or negative. For an infinite hard-core potential, $a > 0$ and is equal to the core size, while $a < 0$ for a repulsive δ-function potential. Hence, from the effective low-energy theory, we expect $a < 0$.

In Fig. 8(b), we show DMRG data for n normalized by $\mu^{1/2}$ as a function of $\mu^{1/2}$ for $N_c = 121$. The magnetization values shown range from $m = m_{\mathrm{FP}} - (3/N_c)$ (three magnons) to $m = 1$ (one magnon per unit cell). To obtain a as a function of λ, we compare the DMRG data with the expression in

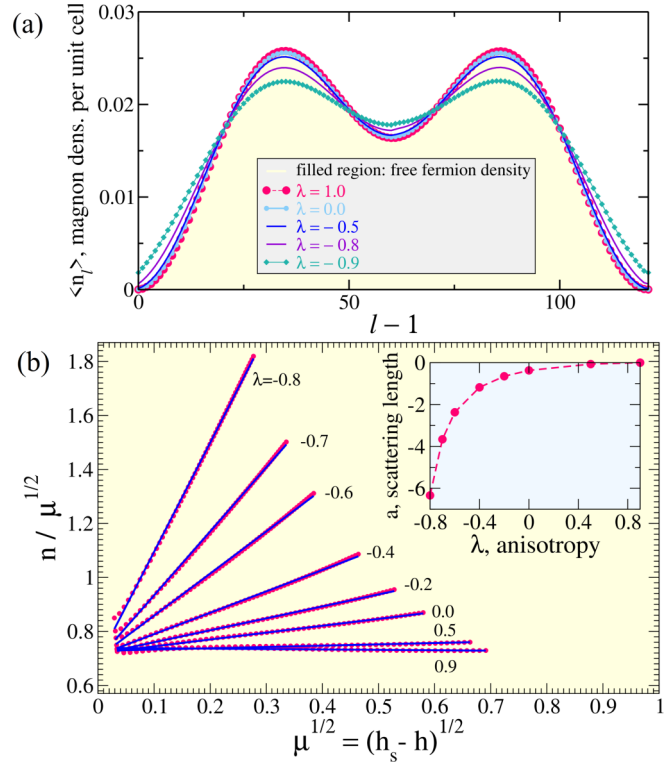

FIG. 8. Dilute magnon regime and the scattering length a, DMRG results for $N_c = 121$. (a) Magnon density $\langle n_l \rangle$ along the chain for two magnons added to the FP state for the indicated values of λ. (b) Average magnon density per unit cell n for the FP plateau: $n = m_{\mathrm{FP}} - m$, with $m_{\mathrm{FP}} = (3/2) + (1/2N_c)$, as a function of $\mu^{1/2}$, where $\mu = h_s - h$ is the effective chemical potential and h_s is the saturation field. Inset: scattering length a derived from a fitting of the DMRG results to the expression of the effective fermion model with a linear correction: $n/\mu^{1/2} = \beta - \frac{4}{3}a\beta^2\mu^{1/2}$, with β and the scattering length a as fitting parameters.

Eq. (17). In fact, from Eq. (17) we find

$$\frac{n}{\mu^{1/2}} = \beta - a\frac{4}{3}\beta^2\mu^{1/2}, \tag{18}$$

with

$$\beta(\lambda) = \sqrt{\frac{2h_s}{\pi^2 v^2}}. \tag{19}$$

We fit the full set of DMRG data in Fig. 8(b) to Eq. (18), for each λ value, by considering β and a as fitting parameters. Indeed, the relative departure between the values of β from the fitting and the ones obtained from Eq. (19) ranges from 5% to 10%. In Fig. 8(b), we observe that $n/\mu^{1/2}$ is almost constant for $\lambda = 0.9$, implying the prevalence of the square-root behavior for these magnetization values. The scattering length a, shown in the inset, is ≈ 0 for $\lambda = 0.9$, and the hard-core boson or free fermion model is thus the most effective theory. Notice that the value of a decreases smoothly as λ decreases and takes only negative values, as expected for a δ-function potential.

VI. SUMMARY AND CONCLUSIONS

In summary, we use the density matrix renormalization group to discuss the phase diagram of the anisotropic AB_2 chain with an applied magnetic field. In particular, we reveal the locus of the magnon edge states, observed in finite-size systems, inside the gap of the topological 1/3 plateau state. In addition, we use the transverse spin correlation functions to estimate the critical point of the Kosterlitz-Thouless transition: $\lambda_{KT} = -0.419 \pm 0.004$ and $h_{KT} = 0.290 \pm 0.002$, such that we reach a better precision than known results. We also display the magnon distribution in the edge states and in the first extended state above the gap. Further, we follow the penetration of the edge states in the bulk as the 1/3 plateau gap closes. The gap closing is also accompanied by an effective squeezing of the chain, parametrized by a boundary scattering length. Considering the bulk states, we also use exact diagonalization to show the topological change in the dispersion relation of the excitations in the vicinity of the Kosterlitz-Thouless transition point. Furthermore, we studied the topologically trivial fully polarized plateau state. Since this insulating state is trivial, we show that the boundary magnon distributions in this case are distinct from that of the excitations from the topological 1/3 plateau state. In particular, we estimate the magnon-magnon scattering length as a function of the anisotropy and confirm that it provides a good correction (linear) to the square-root singularity in the dilute regime of magnons.

We expect that the reported features of the quantum many-body edge and extended states, and the rich phase diagram of the anisotropic Heisenberg AB_2 chain in a magnetic field, notably the KT transition and the topological change of the excitations, will stimulate theoretical and experimental investigations in quasi-one-dimensional compounds exhibiting topological 1/3 magnetization plateaus, including ultracold optical lattice analogs.

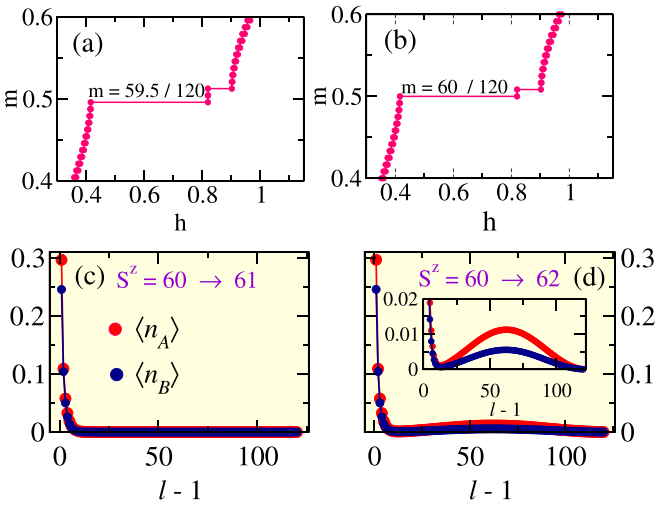

FIG. 9. (a) and (b) DMRG results for $m(h)$ at $\lambda = 0.4$ in the vicinity of the 1/3 plateau magnetization for an even number of unit cells: $N_c = 120$. In (a) we display results for one A site at each boundary, while in (b) we consider one A site at the left boundary and B_1, B_2 sites at the right boundary. (c) One and (d) two magnon excitations above the magnetization $m = 60/120$: average distribution at sites A, $\langle n_A \rangle$, and B, $\langle n_B \rangle \equiv \langle n_{B_1} \rangle + \langle n_{B_2} \rangle$, as a function of the cell position $l - 1$ for the same boundary condition as in (b).

ACKNOWLEDGMENTS

We acknowledge support from Coordenação de Aperfeiçoamento de Pessoal de Nível Superior (CAPES), Conselho Nacional de Desenvolvimento Científico e Tecnológico (CNPq), and Fundação de Amparo à Ciência e Tecnologia do Estado de Pernambuco (FACEPE), Brazilian agencies, including the PRONEX Program, which is funded by CNPq and FACEPE, APQ-0602-1.05/14.

APPENDIX A: MAGNETIZATION FOR AN EVEN NUMBER OF UNIT CELLS

In Fig. 9(a) we show the magnetization $m(h)$ for an even number of unit cells, $N_c = 120$, $\lambda = 0.4$, and the same boundary conditions used throughout the manuscript: one A site at each boundary, with the 1/3-plateau magnetization at $m = (1/2) - (1/2N_c) = 59.5/120$. This curve should be compared with that in Fig. 4(a) for $N_c = 121$. The physical features are essentially identical to that of an odd number N_c, except that for even N_c the minimum value of the spin is $S^z = 1/2$, since the chain has an odd number of sites.

In Fig. 9(b) we show $m(h)$ for a chain with one A site at the left boundary, and B_1, B_2 sites at the right boundary, for $N_c = 120$. In this case, the system presents only one edge state in the left boundary, as shown in Fig. 9(c) through the magnon distribution along the chain. We also show in Fig. 9(d) the first extended magnon excitation. These figures should be compared with the excitations ① → ② and ① → ④ in Fig. 4(b). This behavior can be understood by noticing that there is a "local" distinction between A and B_1, B_2 sites. This is equivalent to the presence of distinct local potentials for A and B_1, B_2 sites, such that this difference inhibits the edge state in the B_1, B_2 boundary.

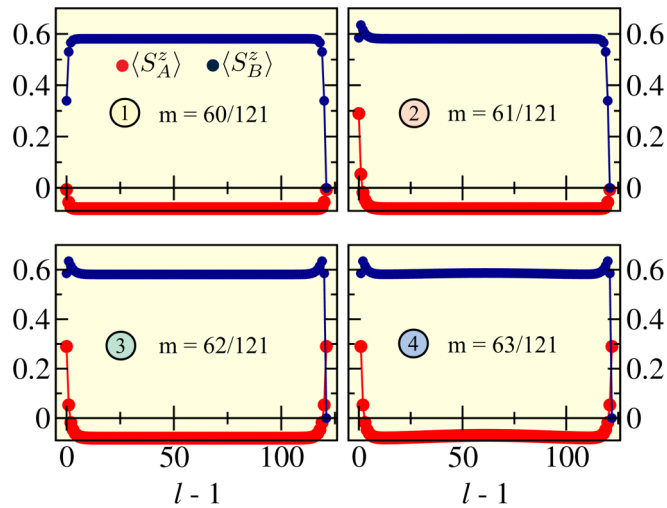

FIG. 10. (a) and (b) DMRG results for the average spin distribution at sites A, $\langle S^z_A \rangle$, and B, $\langle S^z_B \rangle \equiv \langle S^z_{B_1} \rangle + \langle S^z_{B_2} \rangle$, as a function of cell position $l - 1$ at the indicated m-states: ① ($m = 60/121$), ② ($m = 61/121$), ③ ($m = 62/121$), and ④ ($m = 63/121$) for a chain with $N_c = 121$ and $\lambda = 0.4$.

APPENDIX B: AVERAGE LOCAL MAGNETIZATIONS

In Fig. 10 we present the average magnetizations at sites A, $\langle S^z_A \rangle$, and at B sites, $\langle S^z_B \rangle = \langle S^z_{B_1} \rangle + \langle S^z_{B_2} \rangle$ as a function of cell position for $\lambda = 0.4$. These magnetizations were used to build the curves for the average magnon distributions shown in Fig. 4(b), in which case the edge magnon states are highlighted. This is one of the two degenerate states, which is chosen by the renormalization procedure, as explained in the main text.

[1] X.-G. Wen, Choreographed entanglement dances: Topological states of quantum matter, Science **363**, eaal3099 (2019); S. Sachdev, Topological order, emergent gauge fields, and Fermi surface reconstruction, Rep. Prog. Phys. **82**, 014001 (2019).

[2] F. D. M. Haldane, Nobel Lecture: Topological quantum matter, Rev. Mod. Phys. **89**, 040502 (2017).

[3] F. D. M. Haldane, Nonlinear Field Theory of Large-Spin Heisenberg Antiferromagnets: Semiclassically Quantized Solitons of the One-Dimensional Easy-Axis Néel State, Phys. Rev. Lett. **50**, 1153 (1983); F. Haldane, Continuum dynamics of the 1-D Heisenberg antiferromagnet: Identification with the O(3) nonlinear sigma model, Phys. Lett. A **93**, 464 (1983).

[4] W. J. L. Buyers, R. M. Morra, R. L. Armstrong, M. J. Hogan, P. Gerlach, and K. Hirakawa, Experimental Evidence for the Haldane Gap in a Spin-1 Nearly Isotropic, Antiferromagnetic Chain, Phys. Rev. Lett. **56**, 371 (1986); Z. Tun, W. J. L. Buyers, A. Harrison, and J. A. Rayne, Observation of the Haldane gap in $RbNiCl_3$, Phys. Rev. B **43**, 13331 (1991).

[5] S. R. White, Density Matrix Formulation for Quantum Renormalization Groups, Phys. Rev. Lett. **69**, 2863 (1992); Density-matrix algorithms for quantum renormalization groups, Phys. Rev. B **48**, 10345 (1993).

[6] M. Z. Hasan and C. L. Kane, Colloquium: Topological insulators, Rev. Mod. Phys. **82**, 3045 (2010).

[7] X. Chen, Z.-C. Gu, and X.-G. Wen, Complete classification of one-dimensional gapped quantum phases in interacting spin systems, Phys. Rev. B **84**, 235128 (2011); X. Chen, Z.-C. Gu, Z.-X. Liu, and X.-G. Wen, Symmetry protected topological orders and the group cohomology of their symmetry group, *ibid.* **87**, 155114 (2013); R. Verresen, N. G. Jones, and F. Pollmann, Topology and Edge Modes in Quantum Critical Chains, Phys. Rev. Lett. **120**, 057001 (2018).

[8] W. P. Su, J. R. Schrieffer, and A. J. Heeger, Solitons in Polyacetylene, Phys. Rev. Lett. **42**, 1698 (1979).

[9] V. M. Martinez Alvarez and M. D. Coutinho-Filho, Edge states in trimer lattices, Phys. Rev. A **99**, 013833 (2019).

[10] G. Pelegrí, A. M. Marques, R. G. Dias, A. J. Daley, J. Mompart, and V. Ahufinger, Topological edge states and Aharanov-Bohm caging with ultracold atoms carrying orbital angular momentum, Phys. Rev. A **99**, 023613 (2019).

[11] C. L. Kane and T. C. Lubensky, Topological boundary modes in isostatic lattices, Nat. Phys. **10**, 39 (2014).

[12] X. Mao and T. C. Lubensky, Maxwell lattices and topological mechanics, Annu. Rev. Condens. Matter Phys. **9**, 413 (2018).

[13] S. A. Díaz, T. Hirosawa, J. Klinovaja, and D. Loss, Chiral magnonic edge states in ferromagnetic skyrmion crystals controlled by magnetic fields, Phys. Rev. Research **2**, 013231 (2020).

[14] Y. E. Kraus, Y. Lahini, Z. Ringel, M. Verbin, and O. Zilberberg, Topological States and Adiabatic Pumping in Quasicrystals, Phys. Rev. Lett. **109**, 106402 (2012).

[15] L.-J. Lang, X. Cai, and S. Chen, Edge States and Topological Phases in One-Dimensional Optical Superlattices, Phys. Rev. Lett. **108**, 220401 (2012).

[16] M. Oshikawa, M. Yamanaka, and I. Affleck, Magnetization Plateaus in Spin Chains: "Haldane Gap" for Half-Integer Spins, Phys. Rev. Lett. **78**, 1984 (1997).

[17] H. Hu, C. Cheng, Z. Xu, H.-G. Luo, and S. Chen, Topological nature of magnetization plateaus in periodically modulated quantum spin chains, Phys. Rev. B **90**, 035150 (2014); H.-P. Hu, C. Cheng, H.-G. Luo, and S. Chen, Topological incommensurate magnetization plateaus in quasi-periodic quantum spin chains, Sci. Rep. **5**, 8433 (2015).

[18] A. M. S. Macêdo, M. C. dos Santos, M. D. Coutinho-Filho, and C. A. Macêdo, Magnetism and Phase Separation in Polymeric Hubbard Chains, Phys. Rev. Lett. **74**, 1851 (1995).

[19] G.-S. Tian and T.-H. Lin, Quasi-one-dimensional organic unsaturated ferromagnetism: Some rigorous results, Phys. Rev. B **53**, 8196 (1996).

[20] F. C. Alcaraz and A. L. Malvezzi, Critical behavior of mixed Heisenberg chains, J. Phys. A **30**, 767 (1997).

[21] E. P. Raposo and M. D. Coutinho-Filho, Quantum Critical Properties of Ferrimagnetic Hubbard Chains, Phys. Rev. Lett. **78**, 4853 (1997); Field theory of ferrimagnetic Hubbard chains, Phys. Rev. B **59**, 14384 (1999).

[22] R. R. Montenegro-Filho and M. D. Coutinho-Filho, Quasi-one-dimensional quantum ferrimagnets, Physica A **357**, 173 (2005).

[23] M. D. Coutinho-Filho, R. R. Montenegro-Filho, E. P. Raposo, C. Vitoriano, and M. H. Oliveira, Magnetism and electronic correlations in quasi-one-dimensional compounds, J. Braz. Chem. Soc. **19**, 232 (2008).

[24] A. K. Kolezhuk, H.-J. Mikeska, and S. Yamamoto, Matrix-product-states approach to Heisenberg ferrimagnetic spin chains, Phys. Rev. B **55**, R3336 (1997).

[25] S. K. Pati, S. Ramasesha, and D. Sen, Low-lying excited states and low-temperature properties of an alternating spin-1-spin-1/2 chain: A density-matrix renormalization-group study, Phys. Rev. B **55**, 8894 (1997).

[26] K. Maisinger, U. Schollwöck, S. Brehmer, H. J. Mikeska, and S. Yamamoto, Thermodynamics of the (1,1/2) ferrimagnet in finite magnetic fields, Phys. Rev. B **58**, R5908 (1998).

[27] W. M. da Silva and R. R. Montenegro-Filho, Magnetic-field-temperature phase diagram of alternating ferrimagnetic chains: Spin-wave theory from a fully polarized vacuum, Phys. Rev. B **96**, 214419 (2017).

[28] A. S. F. Tenório, R. R. Montenegro-Filho, and M. D. Coutinho-Filho, Quantum phase transitions in alternating spin-(1/2, 5/2) Heisenberg chains, J. Phys.: Condens. Matter **23**, 506003 (2011).

[29] T. Verkholyak, J. Strečka, M. Jaščur, and J. Richter, Magnetic properties of the quantum spin-1/2 XX diamond chain: The Jordan-Wigner approach, Eur. Phys. J. B **80**, 433 (2011).

[30] J. M. Kosterlitz and D. J. Thouless, Ordering, metastability and phase transitions in two-dimensional systems, J. Phys. C **6**, 1181 (1973); J. M. Kosterlitz, The critical properties of the two-dimensional xy model, *ibid.* **7**, 1046 (1974); Kosterlitz-Thouless physics: a review of key issues, Rep. Prog. Phys. **79**, 026001 (2016); Nobel Lecture: Topological defects and phase transitions, Rev. Mod. Phys. **89**, 040501 (2017).

[31] T. Sakai and S. Yamamoto, Critical behavior of anisotropic Heisenberg mixed-spin chains in a field, Phys. Rev. B **60**, 4053 (1999).

[32] G.-H. Liu, L.-J. Kong, and J.-Y. Dou, Haldane magnetization plateau and quantum phase transitions in the spin-(1/2, 1) XXZ chain, Solid State Commun. **213–214**, 10 (2015).

[33] L. M. Veríssimo, M. S. S. Pereira, J. Strečka, and M. L. Lyra, Kosterlitz-Thouless and Gaussian criticalities in a mixed spin-(1/2, 5/2, 1/2) branched chain with exchange anisotropy, Phys. Rev. B **99**, 134408 (2019).

[34] K. Karl'ová, J. Strečka, and M. L. Lyra, Breakdown of intermediate one-half magnetization plateau of spin-1/2 Ising-Heisenberg and Heisenberg branched chains at triple and Kosterlitz-Thouless critical points, Phys. Rev. E **100**, 042127 (2019).

[35] H. Kikuchi, Y. Fujii, M. Chiba, S. Mitsudo, T. Idehara, T. Tonegawa, K. Okamoto, T. Sakai, T. Kuwai, and H. Ohta, Experimental Observation of the 1/3 Magnetization Plateau in the Diamond-Chain Compound $Cu_3(CO_3)_2(OH)_2$, Phys. Rev. Lett. **94**, 227201 (2005); K. C. Rule, A. U. B. Wolter, S. Süllow, D. A. Tennant, A. Brühl, S. Köhler, B. Wolf, M. Lang, and J. Schreuer, Nature of the Spin Dynamics and 1/3 Magnetization Plateau in Azurite, *ibid.* **100**, 117202 (2008); F. Aimo, S. Krämer, M. Klanjšek, M. Horvatić, C. Berthier, and H. Kikuchi, Spin Configuration in the 1/3 Magnetization Plateau of Azurite Determined by NMR, *ibid.* **102**, 127205 (2009); K. C. Rule, M. Reehuis, M. C. R. Gibson, B. Ouladdiaf, M. J. Gutmann, J.-U. Hoffmann, S. Gerischer, D. A. Tennant, S. Süllow, and M. Lang, Magnetic and crystal structure of azurite $Cu_3(CO_3)_2(OH)_2$, Phys. Rev. B **83**, 104401 (2011); H. Jeschke, I. Opahle, H. Kandpal, R. Valentí, H. Das, T. Saha-Dasgupta, O. Janson, H. Rosner, A. Brühl, B. Wolf, M. Lang, J. Richter, S. Hu, X. Wang, R. Peters, T. Pruschke, and A. Honecker, Multistep Approach to Microscopic Models for Frustrated Quantum Magnets: The Case of the Natural Mineral Azurite, Phys. Rev. Lett. **106**, 217201 (2011).

[36] M. Hase, M. Kohno, H. Kitazawa, N. Tsujii, O. Suzuki, K. Ozawa, G. Kido, M. Imai, and X. Hu, 1/3 magnetization plateau observed in the spin-1/2 trimer chain compound $Cu_3(P_2O_6OH)_2$, Phys. Rev. B **73**, 104419 (2006).

[37] K. Morita, M. Fujihala, H. Koorikawa, T. Sugimoto, S. Sota, S. Mitsuda, and T. Tohyama, Static and dynamic magnetic properties of the spin-1/2 inequilateral diamond-chain compounds $A_3Cu_3AlO_2(SO_4)_4$ (A = K, Rb, Cs), Phys. Rev. B **95**, 184412 (2017); M. Fujihala, H. Koorikawa, S. Mitsuda, K. Morita, T. Tohyama, K. Tomiyasu, A. Koda, H. Okabe, S. Itoh, T. Yokoo, S. Ibuka, M. Tadokoro, M. Itoh, H. Sagayama, R. Kumai, and Y. Murakami, Possible Tomonaga-Luttinger spin liquid state in the spin-1/2 inequilateral diamond-chain compound $K_3Cu_3AlO_2(SO_4)_4$, Sci. Rep. **7**, 16785 (2017).

[38] H. Yamaguchi, T. Okita, Y. Iwasaki, Y. Kono, N. Uemoto, Y. Hosokoshi, T. Kida, T. Kawakami, A. Matsuo, and M. Hagiwara, Experimental realization of Lieb-Mattis plateau in a quantum spin chain, Sci. Rep. **10**, 9193 (2020).

[39] S. Yamamoto, S. Brehmer, and H.-J. Mikeska, Elementary excitations of Heisenberg ferrimagnetic spin chains, Phys. Rev. B **57**, 13610 (1998).

[40] E. H. Lieb and W. Liniger, Exact analysis of an interacting Bose gas. I. The general solution and the ground state, Phys. Rev. **130**, 1605 (1963).

[41] I. Affleck, Bose condensation in quasi-one-dimensional antiferromagnets in strong fields, Phys. Rev. B **43**, 3215 (1991).

[42] L. Tonks, The complete equation of state of one, two and three-dimensional gases of hard elastic spheres, Phys. Rev. **50**, 955 (1936); M. Girardeau, Relationship between systems of impenetrable bosons and fermions in one dimension, J. Math. Phys. **1**, 516 (1960).

[43] A. M. Tsvelik, Field-theory treatment of the Heisenberg spin-1 chain, Phys. Rev. B **42**, 10499 (1990).

[44] R. R. Montenegro-Filho and M. D. Coutinho-Filho, Frustration-induced quantum phase transitions in a quasi-one-dimensional ferrimagnet: Hard-core boson map and the Tonks-Girardeau limit, Phys. Rev. B **78**, 014418 (2008).

[45] T. Giamarchi, *Quantum Physics in One Dimension* (Oxford University Press, Oxford, 2004).

[46] T. D. Kühner, S. R. White, and H. Monien, One-dimensional Bose-Hubbard model with nearest-neighbor interaction, Phys. Rev. B **61**, 12474 (2000).

[47] M. A. Griffith and M. A. Continentino, Casimir amplitudes in topological quantum phase transitions, Phys. Rev. E **97**, 012107 (2018); S. Rufo, N. Lopes, M. A. Continentino, and M. A. R. Griffith, Multicritical behavior in topological phase transitions, Phys. Rev. B **100**, 195432 (2019).

[48] J. Lou, S. Qin, T.-K. Ng, Z. Su, and I. Affleck, Finite-size spectrum, magnon interactions, and magnetization of $S = 1$ Heisenberg spin chains, Phys. Rev. B **62**, 3786 (2000).

[49] E. S. Sørensen and I. Affleck, Large-Scale Numerical Evidence for Bose Condensation in the $S = 1$ Antiferromagnetic Chain in a Strong Field, Phys. Rev. Lett. **71**, 1633 (1993); S. Sachdev, T. Senthil, and R. Shankar, Finite-temperature properties of quantum antiferromagnets in a uniform magnetic field in one and two dimensions, Phys. Rev. B **50**, 258 (1994); R. Chitra and T. Giamarchi, Critical properties of gapped spin-chains and ladders in a magnetic field, *ibid.* **55**, 5816 (1997).

[50] K. Okunishi, Y. Hieida, and Y. Akutsu, δ-function Bose-gas picture of $S = 1$ antiferromagnetic quantum spin chains near critical fields, Phys. Rev. B **59**, 6806 (1999).

[51] I. Affleck, W. Hofstetter, D. R. Nelson, and U. Schollwöck, Non-Hermitian Luttinger liquids and flux line pinning in planar superconductors, J. Stat. Mech.: Theor. Exp. (2004) P10003.

[52] I. Affleck, Luttinger liquid parameter for the spin-1 Heisenberg chain in a magnetic field, Phys. Rev. B **72**, 132414 (2005).

[53] L. Vanderstraeten, F. Verstraete, and J. Haegeman, Scattering particles in quantum spin chains, Phys. Rev. B **92**, 125136 (2015).